water

MDPI

Article

A GIS-Based Comparative Analysis of Frequency Ratio and Statistical Index Models for Flood Susceptibility Mapping in the Upper Krishna Basin, India

Uttam Pawar [1], Worawit Suppawimut [2,*], Nitin Muttil [3,4,*] and Upaka Rathnayake [5]

[1] Department of Geography, HPT Arts and RYK Science College, Nashik 422005, Maharashtra, India
[2] Department of Geography, Faculty of Humanities and Social Sciences, Chiang Mai Rajabhat University, Mueang, Chiang Mai 50300, Thailand
[3] Institute for Sustainable Industries & Livable Cities, Victoria University, P.O. Box 14428, Melbourne, VIC 8001, Australia
[4] College of Engineering and Science, Victoria University, P.O. Box 14428, Melbourne, VIC 8001, Australia
[5] Department of Civil Engineering, Faculty of Engineering, Sri Lanka Institute of Information Technology, Malabe 10115, Sri Lanka
* Correspondence: worawit_sup@cmru.ac.th (W.S.); nitin.muttil@vu.edu.au (N.M.)

Abstract: The Upper Krishna Basin in Maharashtra (India) is highly vulnerable to floods. This study aimed to generate a flood susceptibility map for the basin using Frequency Ratio and Statistical Index models of flood analysis. The flood hazard inventory map was created by 370 flood locations in the Upper Krishna Basin and plotted using ArcGIS 10.1 software. The 259 flood locations (70%) were selected randomly as training samples for analysis of the flood models, and for validation purposes, the remaining 111 flood locations (30%) were used. Flood susceptibility analyses were performed based on 12 flood conditioning factors. These were elevation, slope, aspect, curvature, Topographic Wetness Index, Stream Power Index, rainfall, distance from the river, stream density, soil types, land use, and distance from the road. The Statistical Index model revealed that 38% of the area of the Upper Krishna Basin is in the high- to very-high-flood-susceptibility class. The precision of the flood susceptibility map was confirmed using the receiver operating characteristic and the area under the curve value method. The area under the curve showed a 66.89% success rate and a 68% prediction rate for the Frequency Ratio model. However, the Statistical Index model provided an 82.85% success rate and 83.23% prediction rate. The comparative analysis of the Frequency Ratio and Statistical Index models revealed that the Statistical Index model was the most suitable for flood susceptibility analysis and mapping flood-prone areas in the Upper Krishna Basin. The results obtained from this research can be helpful in flood disaster mitigation and hazard preparedness in the Upper Krishna Basin.

Keywords: Upper Krishna Basin; flood susceptibility mapping; frequency ratio; statistical index models; precipitation

Citation: Pawar, U.; Suppawimut, W.; Muttil, N.; Rathnayake, U. A GIS-Based Comparative Analysis of Frequency Ratio and Statistical Index Models for Flood Susceptibility Mapping in the Upper Krishna Basin, India. *Water* **2022**, *14*, 3771. https://doi.org/10.3390/w14223771

Academic Editor: Jianhua Xu

Received: 1 November 2022
Accepted: 18 November 2022
Published: 20 November 2022

1. Introduction

Floods are well-known catastrophic hydro-meteorological disasters that cause huge damage to human life, settlements and industries, agriculture and animals, and the economy [1–7]. Globally, about 170 million people have been affected due to floods every year [8,9]. Under climate change, the frequency and magnitude of floods have increased significantly due to environmental degradation, excessive growth of the population, urbanization, and changing land use pattern [10,11]. According to Alfieri et al. [12], the frequency of floods has increased by over 40% in the last two decades throughout the world, which has caused damages of about 75 billion USD per year. Although measuring the magnitude and reporting the destruction because of inundation are enormously challenging [2], assessments and approximations of floods have significantly increased [13,14]. To minimize

potential losses to the natural and artificial environment because of floods, flood prevention is essential [15]. Therefore, recognizing and plotting flood susceptibility zones significantly help with flood early warning systems, flood management and mitigation, emergency services, and disaster risk reduction [16–19]. Many scholars have conducted studies on Flood Susceptibility Mapping (FSM) using Remote Sensing (RS) and Geographical Information Systems (GISs) for flood hazard analysis [20–27].

The FSM includes environmental, geological, geomorphological, meteorological, topographical factors, and soil characteristics [28–31]. The Logistic Regression (LR), Frequency Ratio (FR), Weight of Evidence (WoE), Statistical Index (SI), Analytical Hierarchy Process (AHP), and Artificial Neural Network (ANN) models have been used by several researchers and government agencies to estimate flood susceptibility precisely [32–39]. Although numerous models have been used for flood susceptibility analysis (FSA), the results obtained by different models varied slightly from region to region. The meteorological and physical characteristics of the river basin are the main factors contributing to floods [40]. Therefore, testing and evaluation of these models can provide optimal and more reliable results [41]. Over the years, statistical methods (LR and SI) have been applied for FSA and natural hazards mapping, and the results of these models are accurate, reliable, and effective for flood disaster management and planning. FR and SI models are simple to run in a GIS environment and can develop valid FSM [27,34,36,37].

India receives more than 75% of its annual rainfall during the monsoon season from June to September [42]. During the monsoon season, flooding in the major rivers of India is the usual phenomenon, for example, the Ganga, Brahmaputra, Narmada, Tapi, Mahi, Godavari, Krishna, and Kaveri Rivers [11,43,44]. According to the NITI Aayog report [45], about 7.17 million hectares of areas of India are affected by floods annually. In addition, about 1.2 million houses are damaged by floods, 1654 human lives are lost, and 618,248 cattle lives are lost annually. The average annual economic losses are Rs 5649 crores. Previous scholars have specified that flood risk zone identification and defensive structural and non-structural risk reduction measures could efficiently decrease flood losses to some extent [46,47]. According to Ullah and Zhang [48], FSM is extensively used to determine flood-prone zones in flood management studies. Therefore, the foremost objective of the present research is a comparative analysis of the FR and SI models for FSM in the Upper Krishna Basin (UKB).

2. Study Area

The Krishna Basin is the second-largest river basin in Peninsular India [49] (refer to Figure 1a). The river has its source near Jor village (Mahabaleshwar) at an elevation of 1337 m in Maharashtra. The river flows for a length of 1400 km and joins the Bay of Bengal in Andhra Pradesh. The Krishna Basin extends over the parts of Maharashtra, Karnataka, Telangana, and Andhra Pradesh. The total area of the Krishna Basin is 2.59 Lakh sq. km. The present study is mainly confined to the UKB up to the Almatti Dam in Karnataka [50] (refer to Figure 1b). The UKB covers parts of Satara, Sangli, and Kolhapur districts in Maharashtra and Belagavi, Bagalkote, and Vijaypura districts in Karnataka (refer to Figure 1c). The catchment area above Almatti dam is approximately 35,925 km^2 [50]. The major tributaries of Krishna in the upper reaches are Koyna, Warna, Panchganga, Dudhganga, and Ghataprabha. The UKB is roughly triangular. It is entirely covered by Deccan trap lava flows. The alluvium mainly occurs along the banks of Krishna River and its major tributaries and thickness vary from 2 to 20 m. The average annual rainfall (AAR) of the UKB is 1347 mm. Nevertheless, annual rainfall varies from 600 mm to 6208 mm. According to the 2011 census, the total population in the UKB occupying three districts in Maharashtra is about 8,170,973 [51]. In the UKB, the Krishna River and its tributaries are susceptible to recurrent flooding during the monsoon season). Some of the recent devastating floods that occurred in the UKB were in 2005, 2006, 2009, 2011, and 2019. Recently, a disastrous flood hit the UKB in August 2019. The list of the locations affected by

the 2019 flood was obtained from various published reports [52,53]. The flood data were classified into training and testing datasets.

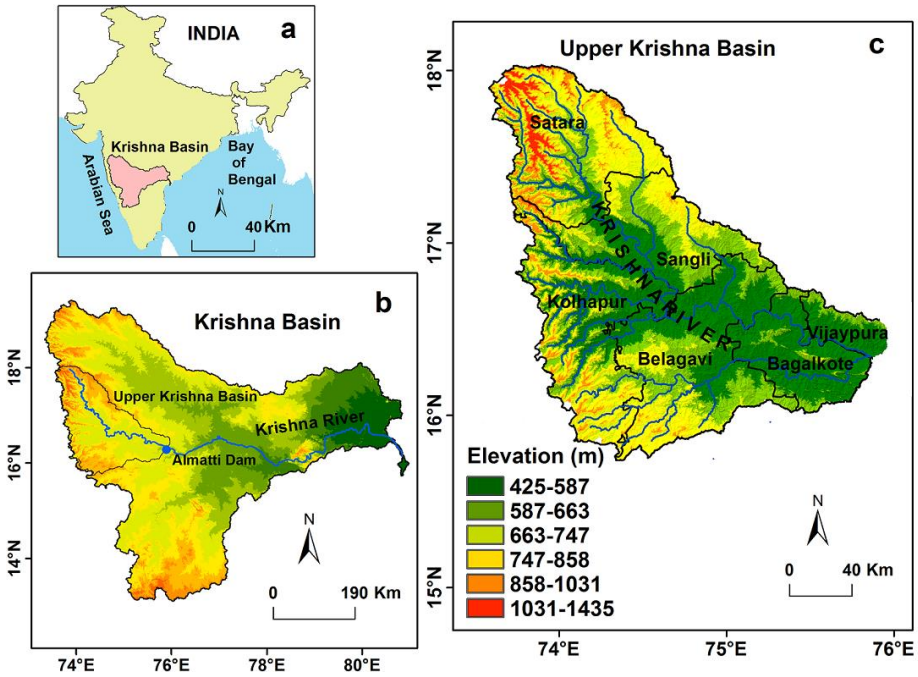

Figure 1. Study area: (**a**) India; (**b**) Krishna Basin; (**c**) Upper Krishna Basin.

3. Materials and Methods

Flood conditioning factors (FCFs) data were obtained from various sources and Table 1 depicts the details. The FSM output was validated by the receiver operating characteristics (ROC) curve. Figure 2 shows a detailed methodology used for FSA.

Table 1. Parameters used for flood susceptibility mapping, their sources, and descriptions.

Flood Conditioning Factors	Data Type	Descriptions	Source
Elevation Slope Aspect Curvature TWI SPI	Raster grid	Derived from ASTER DEM (30 m × 30 m) using ArcGIS	USGS https://earthexplorer.usgs.gov (accessed on 23 August 2022)
Rainfall	Attribute data	Derived from raingauge rainfall data and converted into raster data with 30 m × 30 m cell size	Department of Agriculture, Maharashtra, India Meteorological Department, and Karnataka Sate Natural Disaster Monitoring Center, India
Distance from the river	Vector data (Line)	Derived from stream networks of the UKB (30 m × 30 m) using ArcGIS	USGS https://earthexplorer.usgs.gov (accessed on 23 August 2022)
Stream density	Raster grid	Derived from ASTER DEM (30 m × 30 m) using fill, flow accumulation, drainage density command in ArcGIS	USGS https://earthexplorer.usgs.gov (accessed on 23 August 2022)
Soil types	Vector data (Polygon)	Digital soil map of the world-ESRI shape file	FAO http://www.fao.org (accessed on 22 August)
Land use	Raster grid	Landsat 8 OLI/TIRS, 30 m × 30 m	USGS https://earthexplorer.usgs.gov (accessed on 25 August 2022)
Distance from the road	Vector data (Line)	Derived from road networks of the district and converted into raster data with 30 m × 30 m cell size	DIVA-GIS https://www.diva-gis.org › gdata (accessed on 23 August 2022)
Flood inventory database	Vector data (Point)	Google Earth and Reports	Electronic Media (News), Print Media (Newspaper), Social Media, and Published Reports

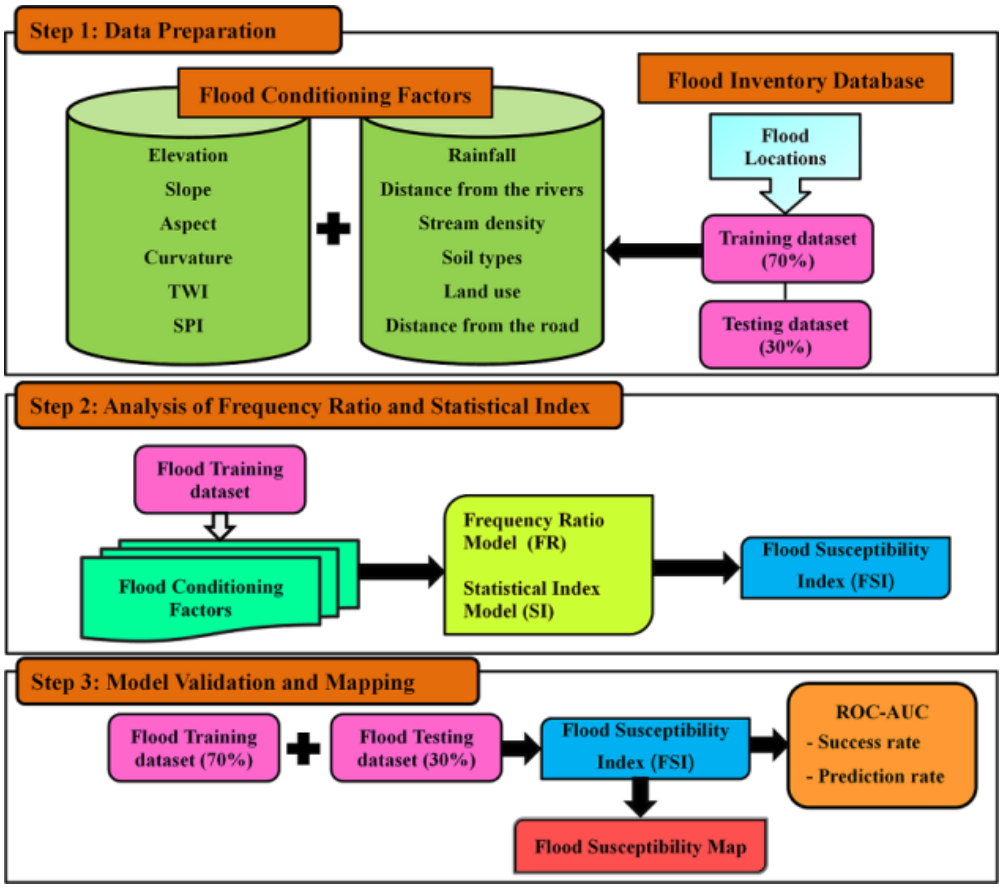

Figure 2. Flow chart of the research methodology.

3.1. Flood Location Data

Flood location data are critical to investigate the association between flood-influencing aspects and flood incidences. The flood inventory map was prepared using the 370 flood locations affected by the August 2019 flood in the UKB (refer to Figure 3). The flood location data were obtained through various reports. The flood sites were classified randomly as training (70%) and (30%) testing sites to build and evaluate the flood models. Accordingly, 259 (111) flood locations were used as training (testing) data.

3.2. Flood Controling Factors

The FCFs were selected based on the area's physical characteristics, data availability, and literature reviews [54–58]. The analyses of the relationship between flood-controlling elements and flood occurrences required a precise flood inventory map [59]. The flood conditioning parameters comprised elevation, slope, aspect, curvature, Topographic Wetness Index (TWI), Stream Power Index (SPI), rainfall, distance from rivers, stream density, soil types, land use, and distance from the road (refer to Table 1). All factors were converted into raster format with 30 × 30 m spatial resolution. The scaling factors (elevation, slope, TWI, SPI, rainfall, stream density, and distance from the rivers and road) were classified into six classes using the natural breaks classification (refer to Figure 4). The elevation is the most recurrently used key factor for FSM. The lower-elevation areas have a high possibility of flooding and are more susceptible to flood disasters [37,60]. The UKB elevation map was prepared using the Digital Elevation Model (DEM) (refer to Figure 4a). The elevation in the UKB stretched between 425 m and 1435 m. According to Souissi et al. [61], the velocity of surface runoff and the infiltration rate of water are affected by the slope. Therefore, ground slope is essential for FSA and FSM (refer to Table 1). The slope of the basin varied from 0 degrees to 70.61 degrees (refer to Figure 4b). The aspect is one of the crucial FCFs [62].

It influences the received rainfall and shows the direction of the maximum slope of the area surface. The aspect map of the UKB was classified into the 9 classes, and the aspect map of the UKB was created in ArcGIS (refer to Figure 4c). Curvature was categorized into three classes: concave, flat, and convex. According to Young and Mutchler [63], a convex slope can generate considerably extra runoff as compared to a concave slope. Hudson and Kesel [64] (2000) revealed that an area with a curvature value from 1.0 to 2.0 is more susceptible to flooding. The curvature map of the UKB was prepared using ArcGIS 10.1 (refer to Figure 4d). TWI represents the cumulative flow at any point within the watershed. It also denotes the spatial distribution of wetness in the basin. TWI has significance in the FSA and flood mapping [24,36,37,54]. TWI was computed using Equation (1) [23,65] and a TWI map was prepared from the DEM in ArcGIS 10.1 (refer to Figure 4e).

$$\mathrm{TWI} = \ln\left[\frac{A_s}{tan\ B}\right] \quad (1)$$

where A_s is the cumulative area to a specific pixel and B is the slope angle in degrees. According to Jebur et al. [66], SPI refers to the rate of the erosive power of surface runoff in a specified site in a river basin and can be given in Equation (2). SPI was reclassified into 6 classes and the SPI map for the UKB was generated in ArcGIS 10.1 software (refer to Figure 4f).

$$\mathrm{SPI} = A_s \times tan\ B \quad (2)$$

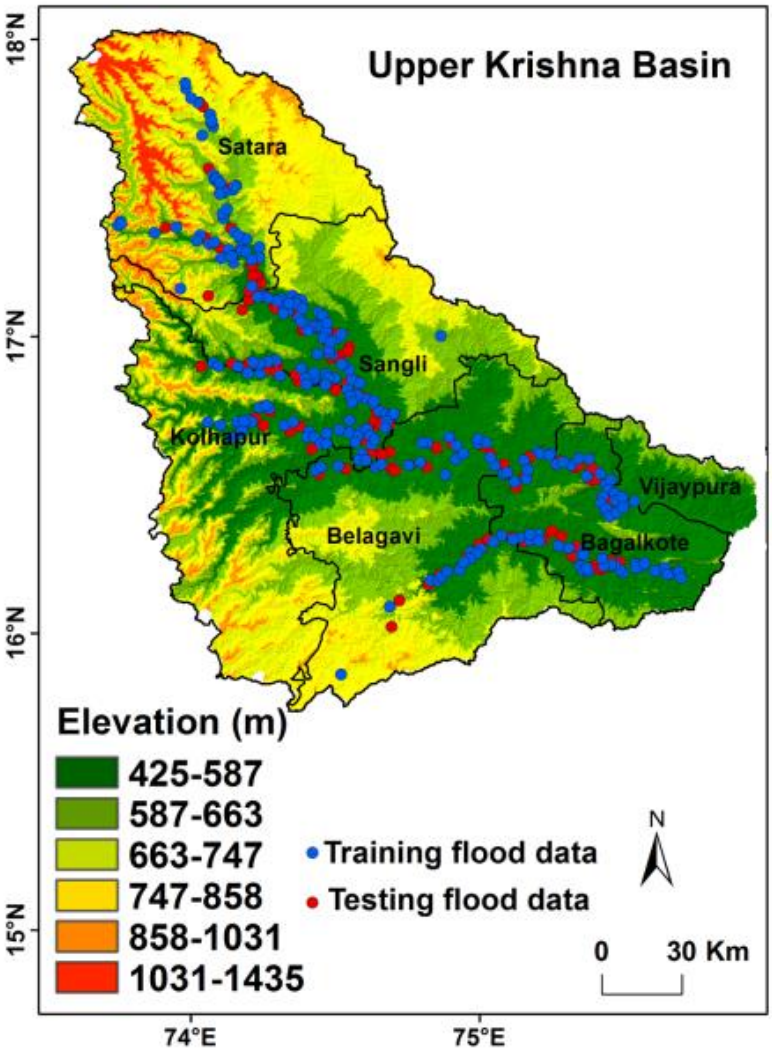

Figure 3. Flood locations in the UKB (August 2019).

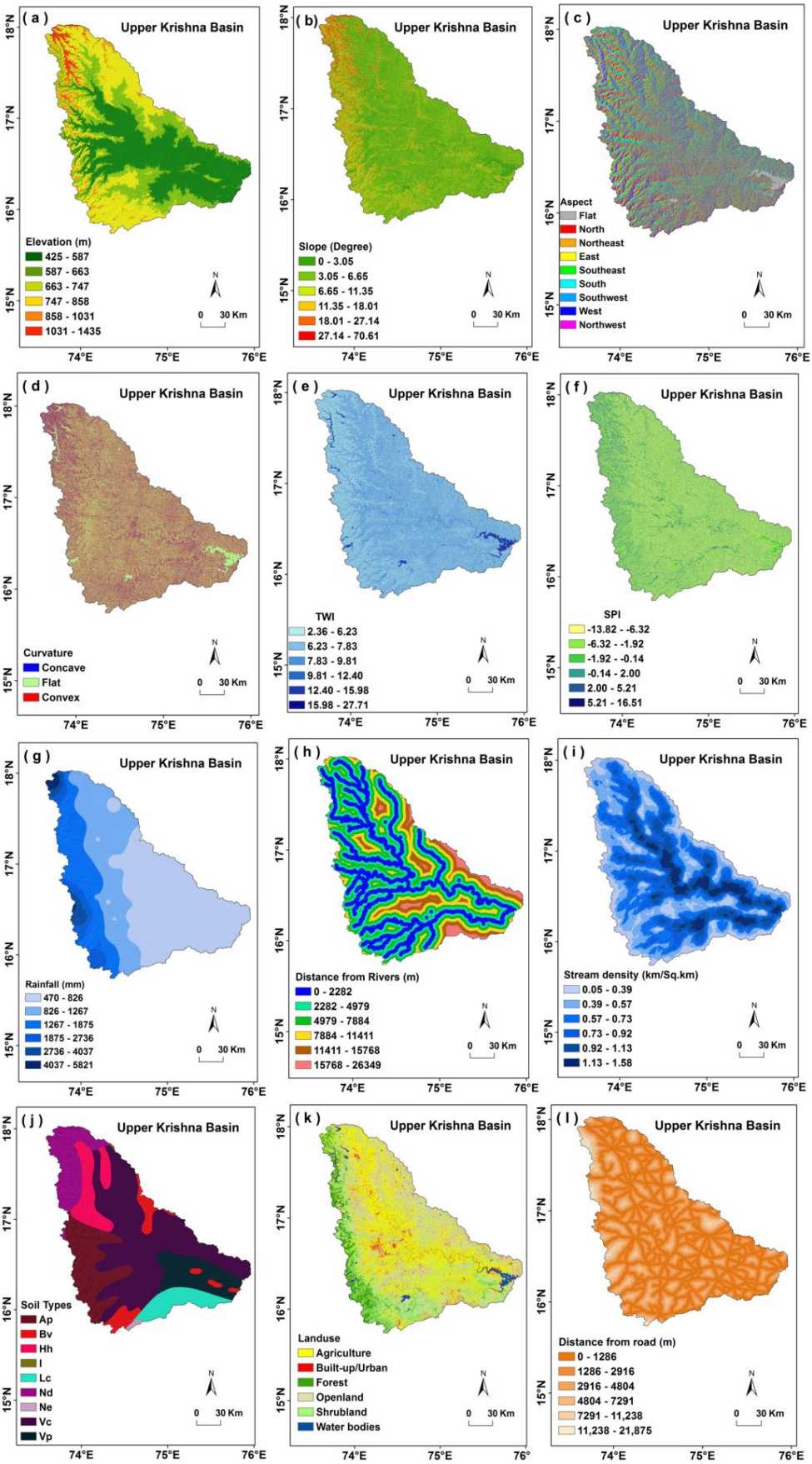

Figure 4. Flood controlling factors used for flood susceptibility analysis.

Rainfall is one of the FCFs that is widely used in flood prediction studies [35,36]. The intensity of rainfall in a short period over an area can cause devastating floods [67]. The long-term rainfall data for the UKB were collected from various sources (refer to Table 1). Several scholars have used the Inverse Distance Weighting (IDW) method for spatial and temporal analysis of rainfall [68,69]. Accordingly, the rainfall distribution map of the UKB based on annual average rainfall (AAR) was prepared (refer to Figure 4g). Distance from the rivers controls the magnitude and spread of floods. There is an inverse relation between the distance from the streams and flood spread [61]. In order to measure distance from the rivers, the Euclidean Distance tool in ArcGIS software was used, and the stream density map of the UKB was generated using the DEM (refer to Figure 4h). According to Shekhar and Pandey [70], the risk of flooding increases when drainage density is high. Accordingly, a stream density map of the UKB was prepared using ArcGIS (refer to Figure 4i). Soil types, texture, and organic matter content affect the rates of surface runoff infiltration in the ground [71,72]. Therefore, the soils in the basin play a significant role in flood magnitude and extent. In addition, the water-holding capacity of soils (soil moisture) depends on the characteristics of soils. Soil type and characteristics were studied from the digital global soil data in shapefile format prepared by the Food and Agriculture Organization (FAO) of the United Nations (refer to Figure 4j). Hölting and Coldewey [73] pointed out that floods are also determined by land cover types. The LC affects surface runoff, infiltration rates, time of concentration of rainwater in the basin, and potential flood extent [74,75]. Nevertheless, areas with dense vegetation cover the decrease in the rate of runoff and increase in the percolation rate, whereas a built-up (urban) area obstructs water intrusion into the ground and accelerates the runoff [76,77]. Therefore, LU data of the UKB were obtained from the Landsat-8 images of the 2021 using random forest classification in the Google Earth Engine platform. The LU data were classified into six classes of land use: agriculture, built-up area, forest land, open land, shrub land, and water bodies (refer to Figure 4k). Lastly, distance from the road was derived with the Euclidean Distance tool in ArcGIS and classified into six categories to determine the distance of specific pixels to the nearest road line (refer to Figure 4l).

3.3. Frequency Ratio (FR) Model

The FR is one of the widely used models in various natural hazard (flood, landslide, and forest fire) analyses and mapping [78–81]. It was used to identify the probabilistic relationship between flood occurrence and FCF. The FR of each conditioning factor class can be expressed as the ratio of the class percentage and the total flood percentage. A greater bivariate probability indicates a stronger correlation, whereas a low *FR* value means a weak correlation. The *FR* value is expressed in Equation (3) as follows [34].

$$FR = \frac{N_{ij}}{P_{ij}} \Big/ \frac{N}{P} \tag{3}$$

where *FR* is the frequency ratio of the sub-classes, N_{ij} is the number of flood locations, P_{ij} is the total number of flood locations in the study area, N is the total number of pixels for each class of the factor, and P is the total number of pixels in the study area. Then, to calculate the flood susceptibility index (*FSI*), the *FR* values of each class were combined following Equation (4).

$$FSI_{FR} = \sum FR \tag{4}$$

where FSI_{FR} is the flood susceptibility index of the *FR* method and $\sum FR$ is the total *FR* values of all classes from each conditioning factor.

3.4. Statistical Index (SI) Model

The statistical index (SI) model was developed by van Westen [82] for landslide susceptibility mapping. SI weight values are calculated using the natural logarithm of the

flood existence in each class of the conditioning factor divided by the total flood density in the study area. The higher positive SI value means a strong relationship between flood occurrence and the class of conditioning factors. The negative value shows the low possibility of flooding the class [83]. In this study, the SI weight values of each class of each conditioning factor were obtained using the following Equation (5) [82].

$$W_{ij} = ln\left(\frac{D_{ij}}{D}\right) = ln\left[\left(\frac{N_{ij}}{S_{ij}} / \frac{N}{S}\right)\right] \quad (5)$$

where W_{ij} is the statistical index value given to the i class of j factors; D_{ij} is the density of floods over the i class of j factor; D is the total density of floods over the entire area; N_{ij} is the number of floods in i class of j factor and is the total number of floods in the study area; S_{ij} is the number of pixels in i class of j factor. N is the total number of flood pixels of the study area and S is the total number of pixels of the study area.

The W_{ij} weights were given to conditioning factors using a reclassification method. Finally, the reclassified factors were summed up to generate the flood susceptibility index (*FSI*) using a raster calculator in the ArcGIS 10.1 software. The *FSI* calculation is shown by the following Equation (6).

$$FSI_{SI} = \sum W_{ij} \quad (6)$$

where FSI_{SI} is the flood susceptibility index of the *SI* method and $\sum W_{ij}$ are the total W_{ij} values of all classes from each conditioning factor.

3.5. Models Validation

Validation is an essential component in natural hazard susceptibility mapping to check the effectiveness and applicability of the model. This study applied the ROC to signify the graphical association of *FSI* and the cumulative percentage of flood occurrence. Frequently, ROC and area under ROC curves (*AUC*) are applied to evaluate the binary response model such as a logistics model [84,85]. They were used for both training data (70%) and testing data (30%). The *AUC* was also used to calculate the success and prediction rates for training and testing data. The computed results were depicted in the percentage of the study area categorized as *FSI* (x-axis) versus the cumulative percent of flood occurrence (y-axis). The *AUC* was calculated using the following equation [86].

$$AUC = \sum_{i=0}^{n}(x_i - x_{i-1})y_i - [\frac{(x_i - x_{i-1})(y_i - y_{i-1})}{2}] \quad (7)$$

where x_i is the percentage of the area and y_i is the area of the flood. *AUC* values vary between a maximum value of 1 or 100% and 0.5 or 50%. According to Silalahi et al. [87], based on the *AUC* value, results can be classified as a very good model (0.9), a good model (0.8–0.9), a medium or reasonable model (0.7–0.8), and a poor model (<0.6).

4. Results and Discussion

4.1. Flood Susceptibility Analysis by the Frequency Ratio Model

The result of the *FR* was obtained for each sub-class of all flood-controlling factors and is summarized in Table 2. Table 2 shows that the maximum (2.31) *FR* value with a high flood area (86.87%) for lower elevation class (425–587 m) proves the high probability of flooding in the lower-elevation area of the UKB. Conversely, zero values of *FR* were observed for the higher elevation classes (858–1031 m and 1031–1435 m) in the basin that signified that these areas have less probability of flooding. Normally, as the elevation increases, the *FR* value decreases, revealing a high positive relation between *FR* and flooding events [35]. The slope of the UKB basin has a relationship with flooding events. The steeper slopes produce runoff more quickly toward the downslope. *FR* values above 1.00 were observed for slopes between 3.05° and 6.65° (1.38) and slopes from 6.65° to 11.35° (1.23), which has

the highest susceptibility to flooding. The maximum flood area (52.12%) was observed for a slope varying between 3.05° and 6.65° in the UKB (refer to Table 2). An *FR* value greater than one is significant for support of flooding [5]. Zero *FR* values were noted for the higher slopes above 18.01°, which have the lowest susceptibility to flooding in the UKB (refer to Table 2). According to Jaiswal et al. [88], a high slope ultimately increases the flood probability of the flood by increasing the swiftness of discharge, and a high-slope area has less time to infiltrate water in the ground. The slope curvature parameter of floods has a significant effect on flood susceptibility. The maximum *FR* values of the aspect parameter of flood control were noted for aspects facing southwest (1.67), west (1.37), and northwest (1.17). Therefore, these slope directions had the greatest control on flood occurrence in the basin (refer to Table 2). The concave slopes had the highest *FR* value (1.17) followed by flat areas with a value of 0.98. About 89% of flood areas were concave and flat in the UKB (refer to Table 2). Khosravi et al. [35] observed maximum flood areas for concave and flat slope areas in the Haraz watershed. In the case of TWI, the first two classes (2.36–6.23 and 6.23–7.83) had an *FR* of more than 1, which revealed a higher probability of flood occurrences in these zones in the UKB (refer to Table 2). Sharif et al. [89] stated that TWI signifies the influence of landscape on the location and extent of saturated source zones in producing surface runoff in a basin. The maximum *FR* value (1.46) was observed for the first class of SPI, which varied between −13.82 and −6.32. However, for the remaining classes, the *FR* was less than one. According to Khosravi et al. [35] the smaller the SPI, the greater the probability of flooding in the basin.

Table 2. Result of the *FR* and SI model for different classes of the factors.

Factors	Class	No. Pixels	Area (%)	Floods Pixels	Flood (%)	Frequency Ratio (*FR*)	Stastical Index (SI)
Elevation (m)	425–587	13685981	37.58	225	86.87	2.31	84
	587–663	9331587	25.62	28	10.81	0.42	−86
	663–747	6918565	19.00	5	1.93	0.10	−229
	747–858	4221014	11.59	1	0.39	0.03	−340
	858–1031	1703324	4.68	0	0.00	0.00	0
	1031–1435	559906	1.54	0	0.00	0.00	0
Slope (degree)	0–3.05	12859597	35.31	69	26.64	0.75	−28
	3.05–6.65	13741170	37.73	135	52.12	1.38	32
	6.65–11.35	5703779	15.66	50	19.31	1.23	21
	11.35–18.01	2382527	6.54	5	1.93	0.30	−122
	18.01–27.14	1226979	3.37	0	0.00	0.00	0
	27.14–70.61	506325	1.39	0	0.00	0.00	0
Aspect	Flat	3989717	10.95	19	7.34	0.67	−40
	North	7311702	20.08	26	10.04	0.50	−69
	Northeast	3589296	9.86	25	9.65	0.98	−2
	East	3794366	10.42	27	10.42	1.00	0
	Southeast	4130598	11.34	36	13.90	1.23	20
	South	3568439	9.80	25	9.65	0.99	−1
	Southwest	3628161	9.96	43	16.60	1.67	51
	West	3274717	8.99	32	12.36	1.37	32
	Northwest	3133381	8.60	26	10.04	1.17	15
Curvature	Convex	3903486	10.72	16	6.18	0.58	−55
	Flat	20857583	57.27	146	56.37	0.98	−2
	Concave	11659308	32.01	97	37.45	1.17	16
Topographic Wetness Index (TWI)	2.36–6.23	11479372	31.52	117	45.17	1.43	36
	6.23–7.83	13937655	38.27	106	40.93	1.07	7
	7.83–9.81	6107429	16.77	25	9.65	0.58	−55
	9.81–12.40	3013928	8.28	7	2.70	0.33	−112
	12.40–15.98	1604271	4.40	4	1.54	0.35	−105
	15.98–27.71	277722	0.76	0	0.00	0.00	0

Table 2. *Cont.*

Factors	Class	No. Pixels	Area (%)	Floods Pixels	Flood (%)	Frequency Ratio (*FR*)	Stastical Index (SI)
Stream Power Index (SPI)	−13.82–−6.32	15348035	42.14	159	61.39	1.46	38
	−6.32–−1.92	5347891	14.68	34	13.13	0.89	−11
	−1.92–−0.14	8268133	22.70	48	18.53	0.82	−20
	−0.14–2.00	4989706	13.70	13	5.02	0.37	−100
	2.00–5.21	2027553	5.57	5	1.93	0.35	−106
	5.21–16.51	439059	1.21	0	0.00	0.00	0
Rainfall (mm)	470–826	16998500	46.67	155	59.85	1.28	25
	826–1267	9985786	27.42	85	32.82	1.20	18
	1267–1875	6621008	18.18	19	7.34	0.40	−91
	1875–2736	1759703	4.83	0	0.00	0.00	0
	2736–4037	777959	2.14	0	0.00	0.00	0
	4037–5821	277421	0.76	0	0.00	0.00	0
Distance from rivers (m)	0–2282	10494750	28.82	226	87.26	3.03	111
	2282–4979	9609658	26.39	27	10.42	0.40	−93
	4979–7884	7927304	21.77	3	1.16	0.05	−293
	7884–11,411	4973052	13.65	2	0.77	0.06	−287
	11,411–15,768	2584543	7.10	1	0.39	0.05	0
	15,768–26,349	831070	2.28	0	0.00	0.00	0
Stream density (km/sq.km)	0.05–0.39	5594652	15.36	2	0.77	0.05	−299
	0.39–0.57	9414604	25.85	3	1.16	0.04	−311
	0.57–0.73	7693109	21.12	13	5.02	0.24	−144
	0.73–0.92	6566155	18.03	55	21.24	1.18	16
	0.92–1.13	4719547	12.96	95	36.68	2.83	104
	1.13–1.58	2432310	6.68	91	35.14	5.26	166
Soil Types	Ap	5527500	15.18	9	3.47	0.23	−147
	Bv	1943925	5.34	1	0.39	0.07	−263
	Hh	3172624	8.71	35	13.51	1.55	44
	l	28852	0.08	0	0.00	0.00	0
	Lc	2468282	6.78	1	0.39	0.06	−287
	Nd	3963555	10.88	6	2.32	0.21	−155
	Ne	120372	0.33	0	0.00	0.00	0
	Vc	15251970	41.88	129	49.81	1.19	17
	Vp	3943297	10.83	78	30.12	2.78	102
Land use	Agriculture	14170930	38.91	51	19.69	0.51	−68
	Built-up/Urban	1431623	3.93	136	52.51	13.36	259
	Forest	2561431	7.03	0	0.00	0.00	0
	Open Land	10295513	28.27	62	23.94	0.85	−17
	Shrub Land	7096236	19.49	10	3.86	0.20	−162
	Water Bodies	863184	2.37	0	0.00	0.00	0
Distance from road (m)	0–1286	12581331	34.54	101	39.00	1.13	12
	1286–2916	11188412	30.72	92	35.52	1.16	15
	2916–4804	7174183	19.70	43	16.60	0.84	−17
	4804–7291	3823147	10.50	20	7.72	0.74	−31
	7291–11,238	1329214	3.65	3	1.16	0.32	−115
	11,238–21,875	324090	0.89	0	0.00	0.00	0

Maximum *FR* values (above 1) were observed for low-AAR classes (from 470 to 1267 mm) and the *FR* was zero for the areas with AAR varying between 1875 mm and 5821 mm in the basin (refer to Table 2). This shows that areas with low AAR are more susceptible to flooding as compared to high-AAR areas in the UKB. The distance from the river flood condition factor denoted that the first class of this parameter had the highest *FR* value (3.03), which suggests that areas from a stream to 2282 m distance are more susceptible to flooding in the UKB (refer to Table 2). In the case of stream density, the high *FR* values (greater than 1) were noted for areas with stream density varying between 0.73 km/sq.km and 1.58 km/sq.km. This specified that areas with high stream density

are more susceptible to flooding than those with less stream density (refer to Table 2). In the UKB, the maximum *FR* value (2.78) was identified for Pellic Vertisols (Vp) followed by Chromic Vertisols (Vc), which was 1.19 (refer to Table 2). Vertisols soils have a high moisture-holding capacity due to the maximum clay content, which varies between 40 and 80% [90,91]. Therefore, the areas of the UKB with Vertisols soils (Vc and Vp) are more vulnerable to flooding than other types of soils. Land use is a very crucial aspect of the FSA of the UKB. A high *FR* value (13.36) was noted for the built-up area with about 53% of the flood area (refer to Table 2). The built-up area increases the surface runoff rate and decreases the infiltration rate. This suggests that growth in the urban or built-up area increases flood susceptibility in the UKB basin. The highest *FR* values for distance from the road were identified for distance classes of 0–1286 m (*FR* = 1.13) and 1286–2986 m (*FR* = 1.16), which denoted high flood susceptibility (refer to Table 2). The FSM of the UKB (refer to Figure 5a) was created by categorizing the *FSI* obtained from the FSA using the *FR* model. The *FSI* was classified into five susceptible zones, namely very low susceptibility, low susceptibility, moderate susceptibility, high susceptibility, and very high susceptibility. A proportion of 3% of the area of the UKB fell in the very-high-susceptibility class, while 12% of the area of the basin fell under the high-susceptibility class. Proportions of 25%, 35%, and 25% of the areas of the basin were identified in the moderate, low, and very low classes of susceptibility, respectively (refer to Figure 5a). Overall, areas with low elevation, low slopes, flat curvature, maximum stream density, maximum TWI, low SPI, near the river, highly urbanized, and covered by Vertisols are more susceptible to flooding in the UKB.

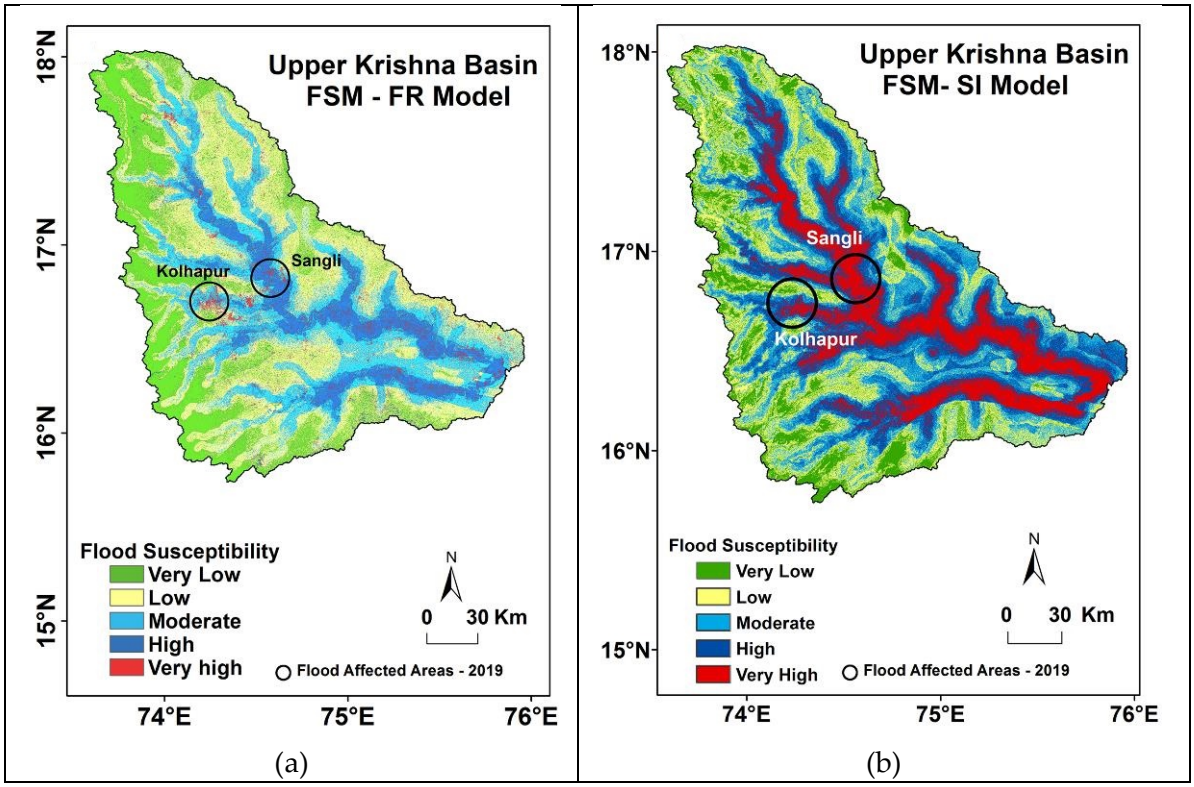

Figure 5. Flood susceptibility maps of UKB: (**a**) based on *FR*; (**b**) based on SI models.

4.2. Flood Susceptibility Analysis by the Statistical Index Model

SI model results are summarized in Table 2. Higher positive SI values specify the maximum possibility of flood incidence, and negative values denote a low chance of flood existence in the region. The highest (84) SI value was noted for heights ranging between 425 and 587, whereas with the elevation increase, the SI values either became negative or zero

(refer to Table 2). A negative SI value (−28) was observed for a varying slope between 0° and 3.05°. The maximum SI values of the slope class 3.05°–6.65° (SI = 32) and 6.65°–11.35° (SI = 21) revealed that areas between these slopes are more susceptible to flooding (refer to Table 2). A positive SI (16) was obtained for the concave curvature, while negative SI values were identified for the convex (−55) and flat (−2) curvatures. This specified that concave surfaces were more vulnerable to flooding in the UKB (refer to Table 2). The highest value of SI (36) was obtained for the TWI flood factor class between 2.36 and 6.23, and negative and zero SI values were found for TWIs above 7.83 (refer to Table 2). For the SPI, the highest SI (38) was obtained for the class of −13.82 to −6.32, and the negative or zero SI values were noted for the rest of the SPI classes (refer to Table 2). In this study, the highest SI (25) value was observed in the lowest rainfall class (470–826 mm), which was the lowland areas in the east of the UKB. The distance from the river of 0–2282 m displayed the highest SI value (111), while other classes were obtained as negative and zero SI values (refer to Table 2). It is obvious that with the increase in distance from the river, the flood possibility decreases [35]. The area with low stream density gained negative SI values (−299, −311, and −144), while the highest SI value (166) was obtained for the stream density class varying between 1.13 and 1.58 km/sq.km (refer to Table 2). According to the soil type factor, the Vertisols soil showed its influence on flood occurrence with high SI values for Vp (SI = 102) and Vc (SI = 17). With the high content of clay and moisture storage, the area with these soil types is more at risk for flooding. In contrast, negative SI values were observed for the Plinthic Acrisols (Ap), Vertic Cambisols (Bv), Chromic Luvisols (Lc), and Dystric Nitosols (Nd) soils (refer to Table 2). In the case of the land use factor, the highest SI (259) was derived for the built-up area (urban), which occupied 13.36% of the flood area, while negative SI values were observed for agricultural land and open land (refer to Table 2). The maximum SI (15) values observed for the second class (1286 m–2916 m) of the distance from the road showed a highly susceptible area for flooding in the basin. Inclusive, all the flood-controlling factors with high SI increased the probability of flood occurrence in the UKB. Likewise, for the *FR* model, the *FSI* was classified into five classes, namely very high, high, moderate, low, and very low (refer to Figure 5b). The FSM generated with the SI model revealed that 16% of the area of the basin was very highly susceptible to floods, whereas 22% of the area of the basin was under a highly susceptible flood zone. The moderate- and low-flood susceptibility classes occupied the same area (25%) of the basin and 13% of the area fell into very low-flood-susceptibility classes (refer to Figure 5b).

4.3. Flood Susceptibility Model Validation and Comparison

Validation of flood susceptibility mapping is essential for flood hazard research. In this research, the *FSI*s obtained from *FR* and SI models were validated to compare their performance. *ROC-AUC* was applied by comparing *FSI* results with training data (70%) and testing data (30%) to generate success and prediction rates (refer to Figure 6). This method is simple and represents a reliable result, frequently used by many flood hazard studies [34,48]. The success and prediction rate curves are portrayed in Figure 6. The *AUC* calculation revealed the 66.89% and 82.85% success rates for *FR* and SI models, respectively. The result of *ROC-AUC* showed 68% and 83.23% prediction rates for the *FR* and SI models, respectively. The results validated by the *AUC* showed an accuracy of the success rate of 82.85% and an accuracy of the prediction rate curve of 83.23%, which specifies a good-quality susceptibility map obtained from the SI model [87]. Therefore, the flood susceptibility map of the UKB obtained by the SI model can be utilized for managing and preventing future flood damages to the people and infrastructure of the UKB.

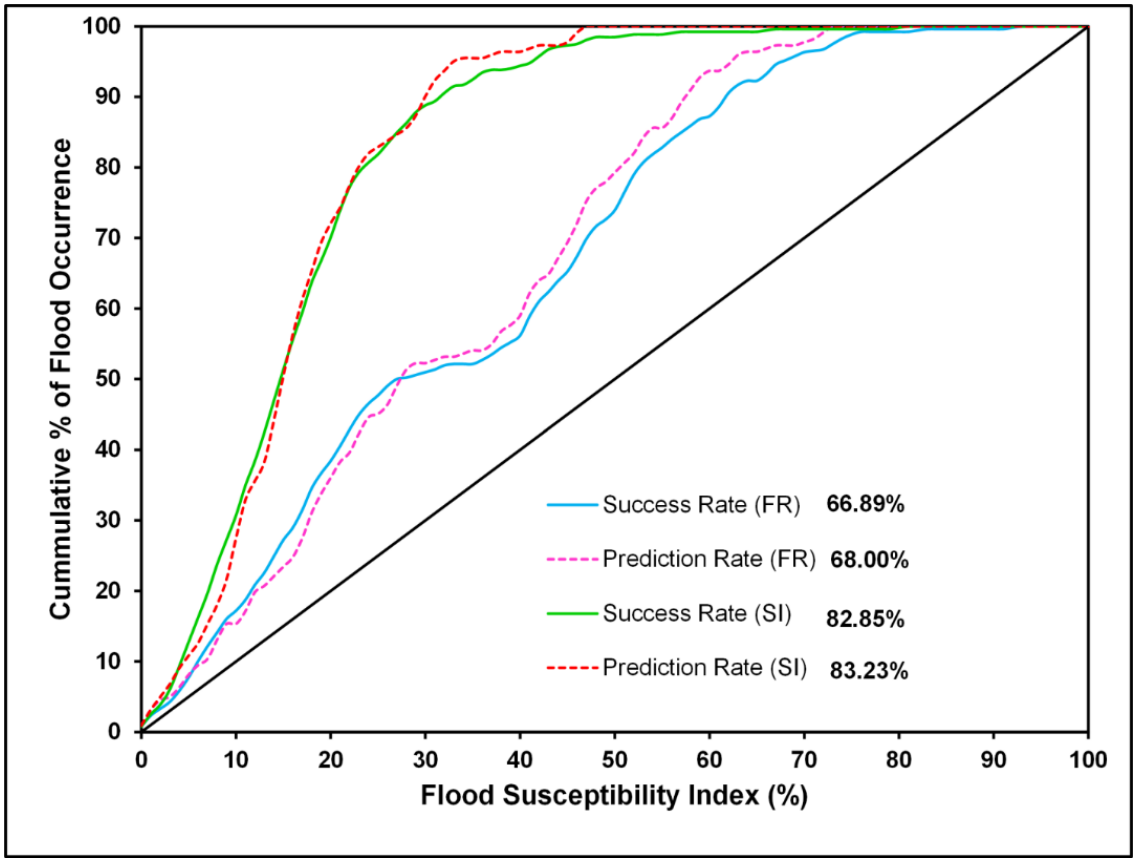

Figure 6. ROC curves of success and prediction rates of the *FR* and SI models.

4.4. Application of the Research

The UKB was severely affected by the disastrous flood in August 2019. Many parts of the Satara, Sangli, and Kolhapur districts in (Maharashtra), and the Belagavi, Bagalkote, and Vijaypura districts (Karnataka) were affected by the flood. The UKB received heavy rainfall from 27 July 2019 to 13 August 2019. Some of the stations located in the UKB recorded nearly 600% (Koyna, Mahabaleshwar) to 1500% (Sangli and Kolhapur) excess rainfall against average normal rain between 27 July and 13 August 2019 (18 days) [52]. Consequently, during a short period, an enormous discharge was produced by the major rivers (Krishna, Warna, and Panchganga) in the Satara, Sangli, and Kolhapur districts in Maharashtra (refer to Figure 7). The Krishna River, Warna River, and Panchganga River in the Sangli and Kolhapur districts became severely flooded on 5–6 August 2019. Extensive inundation in many parts of the Sangli and Kolhapur districts during the August 2019 flood was observed (refer to Figure 8). In the Sangli district, 58 villages covering about 15.17% of the area were affected. In Kolhapur district, 215 villages covering 21.20% of the area were affected [52]. In Sangli and Kolhapur districts, more than one lakh people from 20,000 families were moved to safety by the local people and the National Disaster Response Force (NDRF). About 29 boats in Kolhapur, 43 in Sangli, and 17 boats in Satara were busy evacuating people. In the Kolhapur district, 89 roads were underwater [91]. According to the Vadnere committee report [52], about 1.66 lakh hectares of seasonal and perennial crops were affected in 28 tehsils of Satara, Sangli, and Kolhapur districts. The estimated losses were Rs 3475 crores in these districts [52]. Figure 7 shows that most of the settlements are in the very-high-flood-susceptibility area of the UKB. Therefore, the present study is more beneficial to minimize the losses of infrastructures and settlements, animal and agriculture, and loss of human and animal lives.

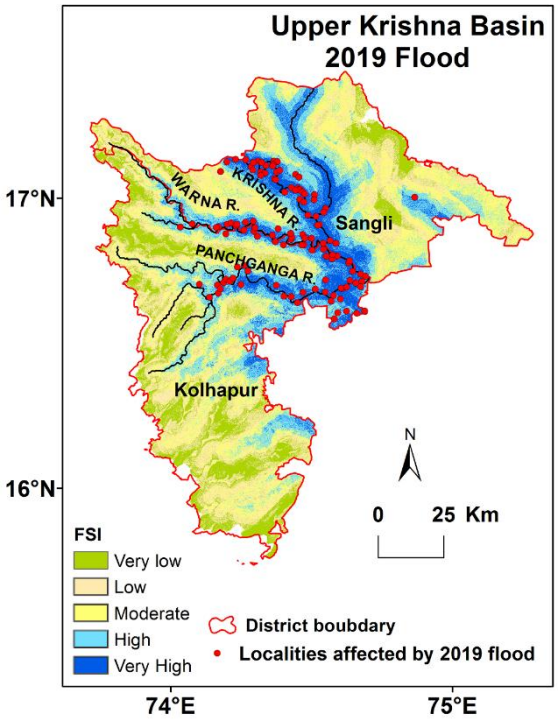

Figure 7. Severely flood-affected areas in Sangli and Kolhapur districts (August 2019).

Figure 8. Clips of 2019 flood in the UKB: (**a**) A view of flooded areas due to overflowing Panchganga River in Kolhapur city (Maharashtra) on 7 August 2019 (PTI). Source: Shivam Bodhe/HT photo. Accessed from: http://www.hindustantimes.com on 27 October 2022; (**b**) a view of flooded areas due to overflowing Krishna River in Sangli on 6–7 August 2019 (PTI). Accessed from: http://indianexpress.com/article on 27 October 2022.

5. Conclusions

The FSM is an essential aspect to understand the scenario of the flood hazard, vulnerability, and risk in hazard management. Therefore, it is indispensable to create the most accurate and trustworthy FSM of the UKB for flood prevention, management, and mitigation. There are several models for flood susceptibility analysis, but *FR* and SI models have been most frequently used in flood modeling [37]. Accordingly, *FR* and SI models were used for flood modeling in the UKB, and the FSM was produced by coalescing all of the weight conditioning factors. The model validation outcomes from *ROC-AUC* denoted that the FSM generated from the SI model is more reliable as compared to the *FR* model. The prediction rate of the SI model (83.23%) was greater than the *FR* model (68%). Therefore, the flood prediction accuracy and superior performance of the SI model are higher than the *FR* model. The FSM maps obtained for the UKB can be significantly supportive

in understanding flood risks, flood possibilities, and flood preparedness to minimize the disastrous effects of floods in the UKB.

Author Contributions: Conceptualization, U.P. and U.R.; methodology, U.P. and W.S.; software, U.P. and W.S.; validation, U.P. and W.S.; formal analysis, U.P. and W.S.; investigation, U.P. and W.S.; resources, U.P.; data curation, U.P.; writing—original draft preparation, U.P. and W.S.; writing—review and editing, U.R. and N.M.; visualization, U.P. and W.S.; supervision, U.R.; project administration, U.R. All authors have read and agreed to the published version of the manuscript.

Funding: This research received no external funding.

Data Availability Statement: Data used in this analysis can be requested from the corresponding author for noncommercial and research purposes.

Conflicts of Interest: The authors declare no conflict of interest.

References

1. Youssef, A.M.; Pradhan, B.; Hassan, A.M. Flash flood risk estimation along the St. Katherine road, southern Sinai, Egypt using GIS based morphometry and satellite imagery. *Environ. Earth Sci.* **2011**, *62*, 611–623. [CrossRef]
2. Du, J.; Fang, J.; Xu, W.; Shi, P. Analysis of dry/wet conditions using the standardized precipitation index and its potential usefulness for drought/flood monitoring in Hunan Province China. *Stoch. Environ. Res. Risk Assess.* **2013**, *27*, 377–387. [CrossRef]
3. Yu, J.; Qin, X.; Larsen, O. Joint Monte Carlo and possibilistic simulation for flood damage assessment. *Stoch. Environ. Res. Risk Assess.* **2013**, *27*, 725–735. [CrossRef]
4. Zou, Q.; Zhou, J.; Zhou, C.; Song, L.; Guo, J. Comprehensive flood risk assessment based on set pair analysis-variable fuzzy sets model and fuzzy AHP. *Stoch. Environ. Res. Risk Assess.* **2013**, *27*, 525–546. [CrossRef]
5. Tehrany, M.S.; Shabani, F.; Jebur, M.N.; Hong, H.; Chen, W.; Xie, X. GIS-based spatial prediction of flood prone areas using standalone frequency ratio, logistic regression, weight of evidence and their ensemble techniques. Geomatics. *Nat. Hazards Risk* **2017**, *8*, 1538–1561. [CrossRef]
6. Pawar, U.V. An Analytical Study of Geomorphological, Hydrological, and Meteorological Characteristics of Floods in the Mahi River Basin: Western India. Ph.D. Thesis, Tilak Maharashtra Vidyapeeth, Pune, India, 2019.
7. Toduse, N.C.; Ungurean, C.; Davidescu, S.; Clinciu, I.; Marin, M.; Nita, M.D.; Davidescu, A. Torrential flood risk assessment and environmentally friendly solutions for small catchments located in the Romania Natura 2000 sites Ciucas, Postavaru and Mare. *Sci. Total Environ.* **2020**, *698*, 134271. [CrossRef]
8. Kazakis, N.; Kougias, I.; Patsialis, T. Assessment of flood hazard areas at a regional scale using an index-based approach and Analytical Hierarchy Process: Application in Rhodope-Evros region, Greece. *Sci. Total Environ.* **2015**, *538*, 555–563. [CrossRef]
9. Wang, Y.; Hong, H.; Chen, W.; Li, S.; Panahi, M.; Khosravi, K.; Shirzadi, A.; Shahabi, H.; Panahi, S.; Costache, R. Flood susceptibility mapping in Dingnan County (China) using adaptive neuro-fuzzy inference system with biogeography based optimization and imperialistic competitive algorithm. *J. Environ. Manag.* **2019**, *247*, 712–729. [CrossRef]
10. Charlton, R.; Fealy, R.; Moore, S.; Sweeney, J.; Murphy, C. Assessing the impact of climate change on water supply and flood hazard in Ireland using statistical downscaling and hydrological modeling techniques. *Clim. Chang.* **2006**, *74*, 475–491. [CrossRef]
11. Pawar, U.V.; Hire, P.S.; Gunjal, R.P.; Patil, A.D. Modeling of magnitude and frequency of floods on the Narmada River: India. *Modeling Earth Syst. Environ.* **2020**, *6*, 2505–2516. [CrossRef]
12. Alfieri, L.; Bisselink, B.; Dottori, F.; Naumann, G.; de Roo, A.; Salamon, P.; Wyser, K.; Feyen, L. Global projections of river flood risk in a warmer world. *Earth's Future* **2017**, *5*, 171–182. [CrossRef]
13. Pradhan, B. Flood susceptible mapping and risk area delineation using logistic regression, GIS and remote sensing. *J. Spat. Hydrol.* **2010**, *9*, 1–18.
14. Diakakis, M.; Mavroulis, S.; Deligiannakis, G. Floods in Greece: A statistical and spatial approach. *Nat. Hazards* **2012**, *62*, 485–500. [CrossRef]
15. Huang, X.; Tan, H.; Zhou, J.; Yang, T.; Benjamin, A.; Wen, S.W.; Li, S.; Liu, A.; Li, X.; Fen, S.; et al. Flood hazard in Hunan province of China: An economic loss analysis. *Nat. Hazards* **2008**, *47*, 65–73. [CrossRef]
16. Dawson, C.W.; Abrahart, R.J.; Shamseldin, A.Y.; Wilby, R.L. Flood estimation at ungauged sites using artificial neural networks. *J. Hydrol.* **2006**, *319*, 391–409. [CrossRef]
17. Bubeck, P.; Botzen, W.; Aerts, J. A review of risk perceptions and other factors that influence flood mitigation behavior. *Risk Anal.* **2012**, *32*, 1481–1495. [CrossRef]
18. Mandal, S.P.; Chakrabarty, A. Flash flood risk assessment for upper Teesta river basin: Using the hydrological modeling system (HEC-HMS) software. *Model. Earth Syst. Environ.* **2016**, *2*, 59. [CrossRef]
19. Bui, D.T.; Ngo, P.T.T.; Pham, T.D.; Jaafari, A.; Minh, N.Q.; Hoa, P.V.; Samui, P. A novel hybrid approach based on a swarm intelligence optimized extreme learning machine for flash flood susceptibility mapping. *Catena* **2019**, *179*, 184–196. [CrossRef]
20. Bates, P.D. Remote sensing and flood inundation modeling. *Hydrol. Process.* **2004**, *18*, 2593–2597. [CrossRef]

21. Liu, J.F.; Li, J.; Liu, J.; Cao, R.Y. Integrated GIS/AHP-based flood risk assessment: A case study of Huaihe River Basin in China. *J. Nat. Disasters* **2008**, *17*, 110–114.
22. Haq, M.; Akhtar, M.; Muhammad, S.; Paras, S.; Rahmatullah, J. Techniques of Remote Sensing and GIS for flood monitoring and damage assessment: A case study of Sindh Province, Pakistan. *Egypt. J. Remote Sens. Space Sci.* **2012**, *15*, 135–141. [CrossRef]
23. Jaafari, A.; Najafi, A.; Pourghasemi, H.; Rezaeian, J.; Sattarian, A. GIS-based frequency ratio and index of entropy models for landslide susceptibility assessment in the Caspian forest, Northern Iran. *Int. J. Environ. Sci. Technol.* **2014**, *11*, 909–926. [CrossRef]
24. Rahmati, O.; Zeinivand, H.; Besharat, M. Flood hazard zoning in Yasooj region, Iran, using GIS and multi criteria decision analysis. *Geomat. Nat. Hazards Risk* **2016**, *7*, 1000–1017. [CrossRef]
25. Paul, G.C.; Saha, S.; Hembram, T.K. Application of the GIS-based probabilistic models for mapping the flood susceptibility in Bansloi sub-basin of Ganga-Bhagirathi river and their comparison. *Remote Sens. Earth Syst. Sci.* **2019**, *2*, 120–146. [CrossRef]
26. Msabi, M.M.; Makonyo, M. Flood susceptibility mapping using GIS and multi-criteria decision analysis: A case of Dodoma region, central Tanzania. *Remote Sens. Appl. Soc. Environ.* **2021**, *21*, 100445. [CrossRef]
27. Suppawimut, W. GIS-Based Flood Susceptibility Mapping Using Statistical Index and Weighting Factor Models. *Environ. Nat. Resour.* **2021**, *19*, 481–493. [CrossRef]
28. Malczewski, J. GIS-based multicriteria decision analysis: A survey of the literature. *Int. J. Geograph. Inform. Sci.* **2006**, *20*, 703–726. [CrossRef]
29. Hwang, C.L.; Lin, M.J. *Group Decision Making under Multiple Criteria: Methods and Applications*; Springer: Berlin/Heidelberg, Germany, 2012.
30. Sarker, S.; Veremyev, A.; Boginski, V.; Singh, A. Critical nodes in river networks. *Sci. Rep.* **2019**, *9*, 11178. [CrossRef]
31. Gao, Y.; Sarker, S.; Sarker, T.; Leta, O.T. Analyzing the critical locations in response of constructed and planned dams on the Mekong River Basin for environmental integrity. *Environ. Res. Commun.* **2022**, *4*, 101001. [CrossRef]
32. Talei, A.; Chua, L.H.C.; Quek, C. A novel application of a neurofuzzy computational technique in event-based rainfall–runoff modeling. *Expert Syst. Appl.* **2010**, *37*, 7456–7468. [CrossRef]
33. Kia, M.B.; Pirasteh, S.; Pradhan, B.; Mahmud, A.R.; Sulaiman, W.N.A.; Moradi, A. An artificial neural network model for flood simulation using GIS: Johor River Basin Malaysia. *Environ. Earth Sci.* **2012**, *67*, 251–264. [CrossRef]
34. Cao, C.; Xu, P.; Wang, Y.; Chen, J.; Zheng, L.; Niu, C. Flash flood hazard susceptibility mapping using frequency ratio and statistical index methods in coalmine subsidence areas. *Sustainability* **2016**, *8*, 948. [CrossRef]
35. Khosravi, K.; Pourghasemi, H.R.; Chapi, K.; Bahri, M. Flash flood susceptibility analysis and its mapping using different bivariate models in Iran: A comparison between Shannon's entropy, statistical index, and weighting factor models. *Environ. Monit. Assess.* **2016**, *188*, 656. [CrossRef]
36. Samanta, S.; Pal, D.K.; Palsamanta, B. Flood susceptibility analysis through remote sensing, GIS and frequency ratio model. *Appl. Water Sci.* **2018**, *8*, 66. [CrossRef]
37. Tehrany, M.S.; Kumar, L.; Jebur, M.N.; Shabani, F. Evaluating the application of the statistical index method in flood susceptibility mapping and its comparison with frequency ratio and logistic regression methods. *Geomat. Nat. Hazards Risk* **2019**, *10*, 79–101. [CrossRef]
38. Hoang, D.V.; Tran, H.T.; Nguyen, T.T. A GIS-based spatial multi-criteria approach for flash flood risk assessment in the Ngan Sau-Ngan Pho mountainous river basin, North Central of Vietnam. *Environ. Nat. Resour. J.* **2020**, *18*, 110–123. [CrossRef]
39. Khaing, T.W.; Tantanee, S.; Pratoomchai, W.; Mahavik, N. Coupling flood hazard with vulnerability map for flood risk assessment: A case study of Nyaung-U Township in Myanmar. *GMSARN Int. J.* **2021**, *15*, 127–138.
40. Şen, Z. *Flood Modelling, Predication and Mitigation*; Springer International Publishing: Cham, Switzerland, 2018. [CrossRef]
41. Shrestha, R.R.; Nestmann, F. Physically based and data-driven models and propagation of input uncertainties in river flood prediction. *J. Hydrol. Eng.* **2009**, *14*, 1309–1319. [CrossRef]
42. Dhar, O.N.; Nandargi, S. Hydrometeorological aspects of floods in India. *Nat. Hazards* **2003**, *28*, 1–33. [CrossRef]
43. Kale, V.S. Monsoon floods in India: A hydro-geomorphic perspective. Flood studies in India. *Geol. Soc. India Mem.* **1998**, *41*, 229–256.
44. Hire, P.S. Geomorphic and Hydrologic studies of Floods in the Tapi Basin. Ph.D. Thesis, University of Pune, Pune, India, 2000.
45. National Institution For Transforming India (NITI). *Report of the Committee Constituted for Formulation of Strategy for Flood Management Works in Entire Country and River Management Activities and Works Related to Border Areas (2021–26)*; National Institution for Transforming: New Delhi, India, 2021.
46. Naulin, J.P.; Payrastre, O.; Gaume, E. Spatially distributed flood forecasting in flash flood prone areas: Application to road network supervision in Southern France. *J. Hydrol.* **2013**, *486*, 88–99. [CrossRef]
47. Guo, E.; Zhang, J.; Ren, X.; Zhang, Q.; Sun, Z. Integrated risk assessment of flood disaster based on improved set pair analysis and the variable fuzzy set theory in central Liaoning Province, China. *Nat. Hazards* **2014**, *74*, 947–965. [CrossRef]
48. Ullah, K.; Zhang, J. GIS-based flood hazard mapping using relative frequency ratio method: A case study of Panjkora River Basin, eastern Hindu Kush, Pakistan. *PLoS ONE* **2020**, *15*, e0229153. [CrossRef] [PubMed]
49. Chanapathi, T.; Thatikonda, S.; Raghavan, S. Analysis of rainfall extremes and water yield of Krishna river basin under future climate scenarios. *J. Hydrol. Reg. Stud.* **2018**, *19*, 287–306. [CrossRef]
50. Rakhecha, P.R.; Deshpande, N.R.; Kulkarni, A.K.; Mandal, B.N.; Sangam, R.B. Design Storm Studies for the Upper Krishna River Catchment Upstream of the Almatti dam site. *Theor. Appl. Climatol.* **1995**, *52*, 219–229. [CrossRef]

51. WRD. *Integrated State Water Plan for Upper Krishna (k-1) Sub-Basin*; WRD: Maharashtra, India, 2015; pp. 1–519.
52. GOM. *Expert Study Committee Report: Floods 2019 (Krishna Basin)*; GOM: Maharashtra, India, 2020; pp. 1–190.
53. GOK. Seeking Central Assistance for Relief and Emergency Works Due to Flood and Landslides in Karnataka during August 2019. In *Memorandum*; GOK: Karnataka, India, 2019; pp. 1–209.
54. Ali, S.A.; Khatun, R.; Ahmad, A.; Ahmad, S.N. Application of GIS-based analytic hierarchy process and frequency ratio model to flood vulnerable mapping and risk area estimation at Sundarban region, India. *Model. Earth Syst. Environ.* **2019**, *5*, 1083–1102. [CrossRef]
55. Chowdhuri, I.; Pal, S.; Chakrabortty, R. Flood susceptibility mapping by ensemble evidential belief function and binomial logistic regression model on river basin of eastern India. *Adv. Space Res.* **2020**, *65*, 1466–1489. [CrossRef]
56. Vafakhah, M.; Mohammad Hasani Loor, S.; Pourghasemi, H.; Katebikord, A. Comparing performance of random forest and adaptive neuro-fuzzy inference system data mining models for flood susceptibility mapping. *Arabian J. Geosci* **2020**, *13*, 11. [CrossRef]
57. Mahato, S.; Pal, S.; Talukdar, S.; Saha, T.; Mandal, P. Field based index of flood vulnerability (IFV): A new validation technique for flood susceptible models. *Geosci. Front.* **2021**, *12*, 101175. [CrossRef]
58. Hasanuzzaman, M.; Adhikary, P.; Bera, B.; Shit, P. Flood vulnerability assessment using AHP and frequency ratio techniques. In *Spatial Modelling of Flood Risk and Flood Hazards*; Springer Nature: Cham, Switzerland, 2022; p. 91. [CrossRef]
59. Pradhan, B.; Tehrany, M.S.; Jebur, M.N. A new semi-automated detection mapping of flood extent from TerraSAR-X satellite image using rule-based classification and Taguchi optimization techniques. *IEEE Trans. Geosci. Remote Sens.* **2016**, *54*, 4331–4342. [CrossRef]
60. Nguyen, V.N.; Yariyan, P.; Amiri, M.; Dang Tran, A.; Pham, T.D.; Do, M.P.; Tien Bui, D. A new modeling approach for spatial prediction of flash flood with biogeography optimized CHAID tree ensemble and remote sensing data. *Remote Sens.* **2020**, *12*, 1373. [CrossRef]
61. Souissi, D.; Zouhri, L.; Hammami, S.; Msaddek, M.H.; Zghibi, A.; Dlala, M. GIS-based MCDM–AHP modeling for flood susceptibility mapping of arid areas, Southeastern Tunisia. *Geocarto Int.* **2020**, *35*, 991–1017. [CrossRef]
62. Bathrellos, G.D.; Skilodimou, H.D.; Soukis, K.; Koskeridou, E. Temporal and spatial analysis of flood occurrences in the drainage basin of Pinios river (Thessaly, Central Greece). *Land* **2018**, *7*, 106. [CrossRef]
63. Young, R.A.; Mutchler, C.K. Effect of slope shape on erosion and runoff. *Trans. ASAE* **1969**, *12*, 0231–0233. [CrossRef]
64. Hudson, P.F.; Kesel, R.H. Channel migration and meander-bend curvature in the lower Mississippi River prior to major human modification. *Geology* **2000**, *28*, 531–534. [CrossRef]
65. Qin, C.Z.; Zhu, A.X.; Pei, T.; Li, B.L.; Scholten, T.; Behrens, T.; Zhou, C.H. An approach to computing topographic wetness index based on maximum downslope gradient. *Precis. Agric.* **2011**, *12*, 32–43. [CrossRef]
66. Jebur, M.N.; Pradhan, B.; Tehrany, M.S. Optimization of landslide conditioning factors using very high-resolution airborne laser scanning (LiDAR) data at catchment scale. *Remote Sens. Environ.* **2014**, *152*, 150–165. [CrossRef]
67. Patil, A.D.; Hire, P.S. Flood hydrometeorological situations associated with monsoon floods on the Par River in western India. *Mausam* **2021**, *71*, 687–698.
68. Pawar, U.; Rathnayake, U. Spatiotemporal rainfall variability and trend analysis over Mahaweli Basin, Sri Lanka. *Arab. J. Geosci.* **2022**, *15*, 370–416. [CrossRef]
69. Pawar, U.; Karunathilaka, P.; Rathnayake, U. Spatio-Temporal Rainfall Variability and Concentration over Sri Lanka. *Adv. Meteorol.* **2022**, *2022*, 6456761. [CrossRef]
70. Shekhar, S.; Pandey, A.C. Delineation of groundwater potential zone in hard rock terrain of India using remote sensing, geographical information system (GIS) and analytic hierarchy process (AHP) techniques. *Geocarto. Int.* **2015**, *30*, 402–421. [CrossRef]
71. Capon, S.J. Flood variability and spatial variation in plant community composition and structure on a large arid floodplain. *J. Arid. Environ.* **2005**, *60*, 283–302. [CrossRef]
72. Chaplot, V.; Poesen, J. Sediment, soil organic carbon and runoff delivery at various spatial scales. *Catena* **2012**, *88*, 46–56. [CrossRef]
73. Hölting, B.; Coldewey, W.G. Surface water infiltration. In *Hydrogeology*; Springer: Berlin/Heidelberg, Germany, 2019; pp. 33–37.
74. Chen, Y.; Liu, R.; Barrett, D.; Gao, L.; Zhou, M.; Renzullo, L.; Emelyanova, I. A spatial assessment framework for evaluating flood risk under extreme climates. *Sci. Total Environ.* **2015**, *538*, 512–523. [CrossRef]
75. Youssef, A.M.; Pradhan, B.; Sefry, S.A. Flash flood susceptibility assessment in Jeddah city (Kingdom of Saudi Arabia) using bivariate and multivariate statistical models. *Environ. Earth Sci.* **2016**, *75*, 1–16. [CrossRef]
76. Hammami, S.; Zouhri, L.; Souissi, D.; Souei, A.; Zghibi, A. Application of the GIS based multi-criteria decision analysis and analytical hierarchy process (AHP) in the flood susceptibility mapping (Tunisia). *Arab. J. Geosci.* **2019**, *12*, 653. [CrossRef]
77. Roslee, R.; Tongkul, F.; Mariappan, S.; Simon, N. Flood hazard analysis (FHAn) using multi-criteria evaluation (MCE) in Penampang Area, Sabah Malaysia. *ASM Sci. J.* **2018**, *11*, 104–122.
78. Yalcin, A.; Reis, S.; Aydinoglu, A.C.; Yomralioglu, T. A GIS-based comparative study of frequency ratio, analytical hierarchy process, bivariate statistics and logistic regression methods for landslide susceptibility mapping in Trabzon, NE Turkey. *Catena* **2011**, *85*, 274–287. [CrossRef]
79. Wu, Y.; Li, W.; Wang, Q.; Liu, Q.; Yang, D.; Xing, M.; Pei, Y.; Yan, S. Landslide Susceptibility Assessment Using Frequency Ratio, Statistical Index and Certainty Factor Models for the Gangu County, China. *Arab. J. Geosci.* **2016**, *9*, 84. [CrossRef]

80. Tiwari, A.; Shoab, M.; Dixit, A. GIS-based forest fire susceptibility modeling in Pauri Garhwal, India: A comparative assessment of frequency ratio, analytic hierarchy process and fuzzy modeling techniques. *Nat. Hazards* **2021**, *105*, 1189–1230. [CrossRef]
81. Rehman, A.; Song, J.; Haq, F.; Mahmood, S.; Ahamad, M.I.; Basharat, M.; Sajid, M.; Mehmood, M.S. Multi-Hazard Susceptibility Assessment Using the Analytical Hierarchy Process and Frequency Ratio Techniques in the Northwest Himalayas, Pakistan. *Remote Sens.* **2022**, *14*, 554. [CrossRef]
82. Westen, C.J.V. *Statistical Landslide Hazard Analysis. ILWIS 2.1 for Windows Application Guide*; ITC Publication: Enschede, The Netherlands, 1997; pp. 73–84.
83. Ali, S.A.; Parvin, F.; Pham, Q.B.; Vojtek, M.; Vojteková, J.; Costache, R.; Thuy Linh, N.T.; Nguyen, H.Q.; Ahmad, A.; Ghorbani, M.A. GIS-Based Comparative Assessment of Flood Susceptibility Mapping Using Hybrid Multi-Criteria Decision-Making Approach, Naïve Bayes Tree, Bivariate Statistics and Logistic Regression: A Case of Topla Basin, Slovakia. *Ecol. Indic.* **2020**, *117*, 106620. [CrossRef]
84. Rossi, M.; Reichenbach, P. LAND-SE: Software for statistically based landslide susceptibility zonation, version 1.0. *Geosci. Model. Dev.* **2016**, *9*, 3533–3543. [CrossRef]
85. Wahono, B.F.D. Applications of statistical and heuristic methods for landslide susceptibility assessments: A case study in Wadas Lintang Sub District, Wonosobo Regency, Central Java Province, Indonesia. Ph.D. Thesis, Gadjah Mada University, Sleman, Indonesia, 2010; pp. 12–37.
86. Pimiento, E. Shallow landslide susceptibility: Modelling and validation. Ph.D. Thesis, Lund University, Lund, Sweden, 2010; pp. 25–29.
87. Silalahi, F.E.S.; Pamela; Arifianti, Y.; Hidayat, F. Landslide susceptibility assessment using frequency ratio model in Bogor, West Java, Indonesia. *Geosci. Lett.* **2019**, *6*, 10. [CrossRef]
88. Jaiswal, R.K.; Mukherjee, S.; Krishnamurthy, J.; Saxena, R. Role of remote sensing and GIS techniques for generation of groundwater prospect zones towards rural development—An approach. *Int. J. Remote Sens.* **2003**, *24*, 993–1008. [CrossRef]
89. Sharif, H.O.; Al-Juaidi, F.H.; Al-Othman, A.; Al-Dousary, I.; Fadda, E.; Jamal-Uddeen, S.; Elhassan, A. Flood hazards in an urbanizing watershed in Riyadh, Saudi Arabia. *Geomat. Nat. Hazards Risk* **2016**, *7*, 702–720. [CrossRef]
90. Dudal, R. *Dark Clay Soils of Tropical and Subtropical Regions*; FAO Agricultural Development Paper No. 83; FAO: Rome, Italy, 1965.
91. De Vos, J.H.; Virgo, K.J. Soil structure in vertisols of the Blue Nile clay plains, Sudan. *Eur. J. Soil Sci.* **1969**, *20*, 189–206. Available online: https://www.thehindu.com/news/national/other-states/floods-paralyse-kolhapur-sangli-132-lakh-evacuated/article28873771.ece (accessed on 27 October 2022). [CrossRef]